

Control of Shock Wave-Boundary Layer Interaction- Induced Separation in Scramjet Inlet Isolator via Fluid Extraction: A Numerical Optimization Study

*A report submitted
in partial fulfillment of the requirements
for the degree of*

Bachelor of Technology

In

Aerospace Engineering

By

- | | |
|---------------------------------|----------------------------|
| 1. B. Neeraj | 2. Divyank Aggarwal |
| (R290221071) | (R290221070) |
| 3. Harshvardhan Bhardwaj | |
| (R290221026) | |



Mechanical Cluster
School of Advanced Engineering (SoAE)
UPES, Dehradun, India – 248007

May 2025



Department of Aerospace

Engineering

UPES

Certificate

It is certified that the work contained in the project titled “**Control of Shock Wave-Boundary Layer Interaction-Induced Separation in Scramjet Inlet Isolator via Fluid Extraction: A Numerical Optimization Study**” by the following students has been carried out under my supervision and that this work has not been submitted elsewhere for a degree.

Student Name

Roll Number

Signature

1. *B. Neeraj*

R290221071

2. *Divyank Aggarwal*

R290221070

3. *Harshvardhan Bhardwaj*

R290221026

Signature

Dr. Kumar Gaurav
(Project Supervisor)

Mechanical Cluster

School of Advanced Engineering

Dehradun, Uttarakhand

India – 248007

Signature

Dr. Ram Kunwar
(Activity Coordinator)

Mechanical Cluster

School of Advanced Engineering

Dehradun, Uttarakhand

India – 248007

Abstract

This study investigates the control of Shockwave-Boundary Layer Interaction (SWBLI) within a hypersonic inlet using high-fidelity Reynolds-Averaged Navier–Stokes (RANS) simulations. SWBLI, particularly in the isolator section of scramjet engines, can lead to boundary layer separation, total pressure loss, and thermal loading, contributing to inlet unstart and reduced engine performance. To address this, a passive flow control strategy using a boundary-layer bleed slot was explored due to its practical feasibility and robustness.

A parametric optimization of the bleed slot was carried out by varying its location, angle, and diameter. The freestream Mach number was maintained at 7.7 throughout all simulations to represent realistic flight conditions. The optimized configuration, located 34.59 mm from the inlet start, with a 60° angle and a diameter of 4.809375 mm , resulting in a significant reduction in the separation bubble height, from 68% to 15% of inlet height, and a 94% decrease in separation area. These improvements were accompanied by enhanced total pressure recovery and flow uniformity.

Acknowledgement

I take this opportunity to express my heartfelt gratitude to my supervisor, **Dr. Kumar Gaurav**, for his invaluable guidance, encouragement, and support throughout the course of this research. His trust in my capabilities and his consistent mentorship created a motivating and productive environment in which I was able to learn and grow both academically and personally. It has been a privilege to work under his supervision.

I am also deeply thankful to the **University of Petroleum and Energy Studies** for providing me with the opportunity to pursue a **Bachelor of Technology in Aerospace Engineering** in a resource-rich and intellectually stimulating environment. The facilities and academic ecosystem at the university played a crucial role in supporting the successful completion of this project.

I would like to extend my sincere thanks to my friends **Khushal Singh, Tripti Vashist, Osama Abdul Karim, Ashutosh, Bhavya Singhal, Lakshya Saxena, Ch. Paritosh, Jasmeet Kaur, Shri Om, and Vikrant Rana** for their constant encouragement, insightful discussions, and companionship throughout this journey.

Finally, I am profoundly grateful to my **parents and family members**, whose unwavering support, patience, and belief in me have been the foundation of all my efforts. Without them, this work would not have been possible.

Names of Students

B. Neeraj

Divyank Aggarwal

Harshvardhan Bhardwaj

Contents

Certificate	ii
Abstract.....	iii
Acknowledgement	iv
List of Figures.....	vii
List of Tables.....	viii
List of Equations	viii
Nomenclature	ix
Chapter 1 Introduction.....	1
1.1 Motivation	2
1.2 Objectives.....	3
1.3 Organization of Report.....	4
Chapter 2 Literature Review	5
2.1 SWBLI: Underlying Flow Physics and Mechanisms	5
2.2 Development and Challenges in SWBLI.....	6
2.3 Controlling the Inevitable.....	7
2.4 Closure.....	8
Chapter 3 Computational Methodology	9
3.1 Geometry.....	9
3.1.1 Baseline Geometry	9
3.1.2 Bleed Slot Geometry	10
3.2 Meshing	11
3.2.1 Baseline Meshing	11
3.2.2 Bleed Slot Meshing	12
3.3 Turbulence Models	12
3.3.1 Reynolds Averaged Navier Stokes (RANS) Model	12
3.3.2 $k - \varepsilon$ Model	13
3.3.3 $k - \omega$ Model.....	13
3.3.4 Shear Stress Transport (SST) $k - \omega$ Model.....	14
3.3.5 Large Eddy Simulation (LES)	14
3.3.6 Detached Eddy Simulation (DES)	15
3.4 Flow Solver.....	15
3.5 Boundary Conditions	15
3.6 Validation of Numerical Model	16

3.6.1 Sensitivity Study	16
3.6.2 Grid Independent Study	17
Chapter 4 Results and Discussion	19
4.1 Baseline Flow Analysis	19
4.2 Bleed Slot Location Optimization	21
4.3 Bleed Slot Angle Optimization	24
4.4 Bleed Slot Diameter Optimization	26
Chapter 5 Conclusion	30
Chapter 6 References	31

List of Figures

Figure No.	Figure Caption	Page No.
1	NASA's X-59 QueSST, and DARPA's HAWC.	3
2	Schlieren Image of SWBLI in High-Speed Inlet, and Oblique Shockwave Boundary Layer Interaction Schematic.	5
3	Start and 3 Unstart Modes in High-Speed Inlets.	6
4	Baseline Geometry recreated from (Fischer & Olivier, 2009).	10
5	Baseline Geometry with Bleed Slot.	11
6	Validation of Numerical Model against Experimental Data from (Fischer & Olivier, 2009).	16
7	Sensitivity Analysis of Numerical Model.	17
8	Grid Independent Study of Numerical Models.	18
9	Mach Contour and Schlieren Image.	19
10	Temperature Contour of Baseline Model and Clipped Temperature Contour with Range (1100K to 1200K).	20
11	Density Contour and Velocity Contour.	20
12	Bleed Slot Location vs π and Bleed Slot Location vs Λ .	22
13	Bleed Location vs Bubble Height, Length, and Area.	23
14	Mach Contour and Magnified Clipped Temperature Contour with Range (1100K to 2100K).	23
15	Bleed Slot Angle vs π and Bleed Slot Angle vs Λ .	24
16	Bleed Angle vs Bubble Height, Length, and Area.	25
17	Mach Contour and Magnified Clipped Temperature Contour with Range (1100K to 2100K).	26
18	Bleed Slot Diameter vs π and Bleed Slot Diameter vs Λ .	27
19	Bleed Diameter vs Bubble Height, Length, and Area.	28
20	Mach Contour and Magnified Clipped Temperature Contour with Range (1100K to 2100K).	29

List of Tables

Table No.	Table Caption	Page No.
1	Bleed Slot Locations	21
2	Bleed Slot Angles	24
3	Bleed Slot Diameter	26

List of Equations

Equation No.	Equation Caption	Page No.
1	Reynolds Averaging	12
2	Continuity Equation	12
3	Momentum Equation	13
4	Energy Equation	13
5	Boussinesq Hypothesis	13
6	Turbulent Viscosity relation to k and ω	13
7	Turbulent Kinetic Energy	14
8	Dissipation Rate per unit Turbulence Kinetic Energy	14

Nomenclature

α	Model Constant; Empirical Value = $5/9$
β	Model Constant; Empirical Value = $3/40$
β^*	Model Constant; Empirical Value = $9/100$
σ_k	Turbulent Kinetic Energy Prandtl Number; Empirical Value = 2.0
σ_ω	Specific Dissipation Rate Prandtl Number; Empirical Value = 2.0
e_t	Internal Energy (J)
ρ	Density (kg/m ³)
$\bar{\rho}$	Density Time Average Component
ρ'	Fluctuating Density
U	Velocity (m/s)
\bar{U}	Velocity Time Average Component
u'	Fluctuating Velocity
P	Pressure (Pa)
\bar{P}	Pressure Time Average Component
p'	Fluctuating Pressure
t	Time (s)
\vec{V}	Velocity Vector
T	Temperature (K)
$\bar{\tau}$	Stress Tensor
k	Turbulent Kinetic Energy
ε	Turbulent Dissipation Rate
μ_t	Turbulent Viscosity
ω	Dissipation Rate per unit Turbulence Kinetic Energy or Specific Dissipation Rate
C_p	Constant Pressure
π	Total Pressure Recovery (Outlet Total Pressure/Inlet Total Pressure)
Λ	Mass Flow Rate Ratio (Bleed Outlet Mass Flow Rate/Inlet Mass Flow Rate)
SWBLI	Shock Wave-Boundary Layer Interaction
AJVGs	Air-Jet Vortex Generator
MVG	Micro-Vortex Generator
CVPs	Counter-Rotating Vortex Pairs
SSB	Small Separation on the Body Side
LSB	Large Separation on the Body Side
DSBL	Dual-Separation on both Body and Lip
RANS	Reynolds-Average Navier-Stokes
LES	Large Eddy Simulation
DES	Detached Eddy Simulation
AUSM	Advection Upstream Splitting Methods
SST	Shear Stress Transport
RNG	Renormalization Group
SGS	Sub-Grid Scale

Chapter 1

Introduction

The interaction between shockwaves and boundary layers, known as Shockwave–Boundary Layer Interaction (SBLI), has been a fundamental area of study since the earliest efforts to understand and achieve supersonic and hypersonic flight. Previous studies reveal that SBLI is a defining characteristic that governs the flow’s behaviour and stability (Babinsky & Harvey, 2011; Bogdonoff et al., 1953; Curran & Murthy, 2000).

SBLI occurs when a shockwave forms near a solid surface with a boundary layer. Shockwaves create a significant and discontinuous increase in the flow’s pressure (Babinsky & Harvey, 2011). However, in the case of SBLI, this pressure rise is weakened due to the presence of the boundary layer (Green, 1970). The pressure rise generated downstream of the shock is communicated upstream through the subsonic region adjacent to the wall (Xu et al., 2022). In response, the upstream boundary layer thickens to remain attached (Sabnis & Babinsky, 2023). However, it completely detaches for a sufficiently high adverse pressure gradient, leading to flow separation.

The thickening of the boundary layer displaces the streamlines outside the boundary layer, generating pressure waves. These pressure waves interact with the shockwave, modifying its structure and, as a result, altering the information being propagated upstream through the subsonic channel (Green, 1970). This interaction creates a feedback loop that further complicates the dynamics of SBLI (Sabnis & Babinsky, 2023).

Early research established the crucial role of boundary layer properties in SBLI, while also revealing significant gaps in the predictive models (Delery, 1985; Dolling, 2001; Green, 1970). Later work demonstrated that isolator length improves inlet stability up to a limit (Reinartz et al., 2003), wall temperature influences separation behavior (Fischer & Olivier, 2009), and stronger interactions lead to greater low-frequency unsteadiness (Souverein et al., 2010). Studies of hypersonic inlets showed the influence of the angle-of-attack on flow choking and oscillatory unstarts (Xu et al., 2022), and that separate flow modes such as LSB, SSB, and DSBL govern inlet stability (Tang et al., 2023). High-quality experimental data on compression ramps at Mach 6.5 to 8.3 (Lara et al., 2023) and improved numerical validation (Park et al., 2023) have further developed SBLI modelling.

Recent efforts focus on controlling SBLI-induced separation and preventing unstart in hypersonic inlets. Flow control strategies are broadly categorized into passive and active methods.

Passive control techniques modify surface properties or introduce geometric elements. Methods such as micro-vortex generators (MVGs) and micro-ramps generate streamwise vortices that re-energize the boundary layer, preventing separation and stabilizing the flow at high speeds (Babinsky et al., 2009; Wang et al., 2022; Zhang et al., 2025). Recent numerical studies showed that mixed-orientation vortex generator arrays performed better than single-orientation layouts (Khan et al., 2024). Herringbone riblets, inspired by sharks and birds, produced small but notable reductions in separation (Wen et al., 2024). Studies also reveal that smoother surfaces weaken SBLI, decreasing boundary layer thickness and

separation (Garcia et al., 2022). Boundary-layer Bleed method removes low-momentum fluid, reducing shock-induced separation and thermal loads, stabilizing the flow, and increasing inlet performance (Reinartz et al., 2003).

Active flow control techniques inject energy into the flow to actively manipulate separation and shock structures. Air-jet vortex generators (AJVGs) and microjet arrays inject high-momentum flow to generate counter-rotating vortex pairs (CVPs), which energize the boundary layer and reduce separation length, with enhanced effectiveness at Mach Numbers above 2.7 (Ramaswamy & Schreyer, 2021; Sebastian & Schreyer, 2023; Wang et al., 2022). Spanwise-inclined AJVG configurations have proven to be flexible for both supersonic and hypersonic flows (Ramaswamy & Schreyer, 2021; Sebastian & Schreyer, 2023), while optimal intermediate jet spacing offers improved flow control effectiveness (Wang et al., 2022).

Overall, while passive methods offer simplicity and robustness, active methods deliver dynamic adaptability at the cost of greater complexity and energy demands (Gaitonde, 2015).

Each flow control technique presents unique advantages, yet none are without inherent limitations. In this paper, a detailed analysis of the bleed slot configuration is performed to identify an optimized solution that offers enhanced performance. While bleed-based control remains one of the most practical and robust methods for managing SBLI, there has been limited progress in optimizing bleed slot design. This study seeks to advance both the understanding and application of bleed slot strategies, contributing to the ongoing evolution of high-speed flow control technologies.

1.1 Motivation

The demand for advanced high-speed aerospace systems, such as hypersonic vehicles, scramjets, reusable space access platforms, and next-generation defence technologies, has significantly risen in recent years. As these platforms operate at extreme velocities, SWBLI emerges as a critical phenomenon affecting aerodynamic efficiency, structural integrity, propulsion stability, and overall mission performance. Uncontrolled SWBLI leads to severe flow separation, thermal loading, and inlet unstart, which can compromise vehicle performance and safety. Given the resurgence of global interest in hypersonic technology, as evidenced by intensified research programs such as DARPA's Hypersonic Air-breathing Weapon Concept (HAWC), NASA's X-59 QueSST, and international developments in hypersonic glide vehicles, as illustrated in Figure 1. A deep understanding of SWBLI and its mitigation strategies is more vital than ever.



Figure 1 NASA's X-59 QueSST (Born To Engineer) on left, and DARPA's HAWC (Air Force Technology) on right

Flow control methods designed to manage SWBLI play an indispensable role in enabling reliable and efficient operation at high Mach numbers. However, despite decades of research, achieving robust and energy-efficient control remains a significant technical challenge. Many traditional techniques, while conceptually effective, are often constrained by practical limitations in real-world operational environments.

This research aims to contribute to addressing this gap by advancing the understanding of SWBLI phenomena and evaluating flow control strategies that offer a balance between aerodynamic performance improvement and system feasibility. By refining these techniques, this work seeks to support the design of future aerospace vehicles capable of safer, more efficient, and more sustainable hypersonic flight.

1.2 Objectives

Objective 1: To Comprehend the Physical Phenomena Involved in Shockwave Boundary Layer Interactions (SWBLI) Encountered in Scramjet Inlets.

Objective 2: To Predict the Flow Behavior and Associated Phenomena in 2D SWBLI Using High-Fidelity Simulations.

Objective 3: To Investigate the Effectiveness of Active Flow Control Methods (MVG, AJVG, and Boundary Layer Bleed) for Shock-Induced Separation.

SWBLI can lead to boundary layer thickening, the formation of strong adverse pressure gradients, flow separation, and intensification of thermal loads within the scramjet inlets. A thorough understanding of the underlying interaction mechanisms—particularly shock-induced separation, reattachment behavior, and separation bubble dynamics—is essential for accurately predicting performance degradation and developing mitigation strategies. This investigation focuses primarily on the isolator regions of scramjet inlets, where confined SWBLI often results in flow choking and inlet unstart.

High-fidelity Reynolds-averaged Navier–Stokes (RANS) simulations are employed to capture the complex flow features while maintaining practical computational efficiency. The computational framework utilizes second-order accurate Advection Upstream Splitting Methods (AUSM) for flux calculations and structured grids to ensure accurate shock capturing and turbulence resolution. Two-dimensional geometries, representative of

compression ramps and isolator configurations, are analyzed to investigate shock-induced separation, reattachment points, separation bubble size, and wall pressure distributions.

While multiple active flow control methods, including MVG and AJVG, are reviewed and conceptually evaluated in this study, the primary focus is directed toward the optimization of boundary-layer bleed slot configurations. Key parameters such as bleed slot diameter, location, and inclination angle are systematically varied to determine their influence on flow stabilization and separation suppression. This targeted investigation aims to identify bleed configurations that maximize separation bubble reduction, enhance total pressure recovery, and improve inlet flow uniformity, thereby advancing the design and operability margins of hypersonic inlets.

1.3 Organization of Report

This report is organized into six chapters, each addressing a specific aspect of the study on Shock Wave–Boundary Layer Interaction (SWBLI) and the optimization of bleed slot geometry for flow control in hypersonic inlets.

Chapter 1: Introduction: This chapter introduces the background and significance of SWBLI in high-speed flows. It outlines the motivation behind the research, defines the objectives of the study, and presents the overall structure of the report.

Chapter 2: Literature Review: This section provides a comprehensive overview of the existing research on SWBLI. It discusses the fundamental flow physics, historical development, ongoing challenges, and various flow control strategies used to manage this inherently complex phenomenon.

Chapter 3: Computational Methodology: This chapter details the numerical framework used in the study, including the geometry configurations, mesh generation, turbulence models, governing equations, boundary conditions, and solver settings. It also includes the baseline validation against experimental data and a sensitivity and mesh independence analysis.

Chapter 4: Results and Discussion: The core findings of the study are presented and analyzed in this chapter. It begins with baseline flow behavior and proceeds through a three-stage optimization process for bleed slot distance, angle, and diameter. The effects of each parameter on separation control and pressure recovery are discussed in depth.

Chapter 5: Conclusion: This chapter summarizes the key outcomes of the research, highlighting the most effective bleed configuration and its implications for SWBLI control in scramjet inlets.

Chapter 6: References: A complete list of scholarly works and technical documents cited throughout the report is provided for reference and further reading.

Chapter 2

Literature Review

2.1 SWBLI: Underlying Flow Physics and Mechanisms

SWBLI occurs when a shockwave forms near a solid surface along which a boundary layer is present. In an ideal inviscid flow, a shockwave produces a sharp, discontinuous rise in the flow's pressure, density, and temperature (Babinsky & Harvey, 2011). However, in the presence of a boundary layer, the pressure rise is weakened and diffused, primarily due to the viscous and thermal effects associated with the near-wall flow (Green, 1970). The pressure increase generated downstream of the shock is communicated upstream through a subsonic layer located adjacent to the wall, a phenomenon enabled by the fact that the near-wall region remains subsonic even in otherwise supersonic flows (Xu et al., 2022). Upon receiving this upstream-propagated pressure signal, the boundary layer thickens in an attempt to adjust to the adverse pressure gradient and remain attached to the surface (Sabnis & Babinsky, 2023). However, if the imposed pressure gradient exceeds a critical limit, the boundary layer can no longer maintain attachment and undergoes separation, creating a separated shear layer downstream. The separation phenomenon is illustrated in Figure 2.

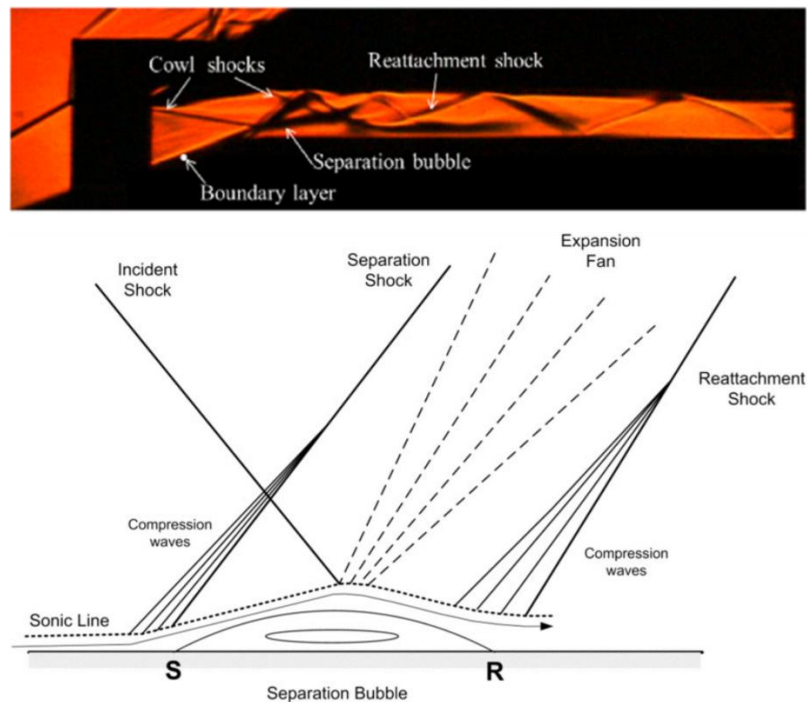


Figure 2 Top Image: Schlieren Image of SWBLI in High-Speed Inlet; Bottom Image: Oblique Shockwave Boundary Layer Interaction Schematic (Sabnis & Babinsky, 2023; Sepahi-Younsi et al., 2019)

The thickening of the boundary layer causes displacement of the external streamlines away from the wall, generating pressure disturbances. These disturbances subsequently interact with the shockwave, modifying its position and strength (Green, 1970). As a result, the information traveling through the subsonic channel upstream is altered, setting up a complex feedback loop between the shock system and the boundary layer (Sabnis & Babinsky, 2023). This feedback mechanism significantly influences the stability and

dynamics of SWBLI, often leading to highly unsteady and broadband low-frequency oscillations in practical applications. Understanding and predicting this coupled interaction remain central challenges in high-speed aerodynamics.

2.2 Development and Challenges in SWBLI

Early investigations into SWBLI established the influence of boundary layer properties, such as thickness, turbulence intensity, and state of development, on the behavior of the interaction (Babinsky & Harvey, 2011; Green, 1970; Sabnis & Babinsky, 2023). These studies also revealed shortcomings in existing predictive models, particularly under conditions involving turbulent boundary layers, strong shocks, and complex three-dimensional effects (Gaitonde, 2015). Following research demonstrated that geometrical factors, such as the length of the isolator section in scramjet inlets, play a pivotal role in flow stability, i.e., while longer isolators improve stability by allowing shock systems more space to be regulated, they also introduce additional viscous losses (Reinartz et al., 2003). Investigations further showed that wall temperature has a strong influence on separation behavior, with elevated wall temperatures worsening separation (Fischer & Olivier, 2009). Moreover, it was found that stronger interactions correspond to greater low-frequency unsteadiness in the shock-boundary layer system (Souverein et al., 2010), complicating flow control strategies.

In the realm of hypersonic inlet research, studies revealed that variations in the angle of attack can cause flow choking and trigger oscillatory inlet unstarts (Tang et al., 2024). Additionally, distinct unstart modes, including large separation on the body side (LSB), small separation on the body side (SSB), and dual-separation modes (DSBL), illustrated in Figure 3, were identified as critical determinants of inlet stability (Tang et al., 2023).

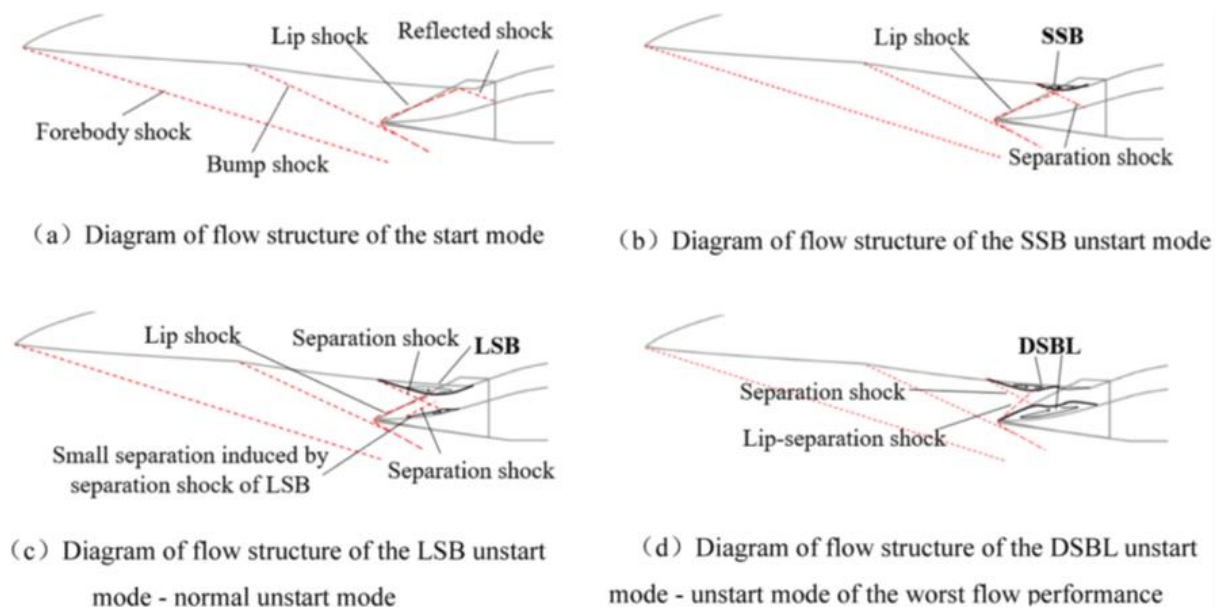


Figure 3 Start and 3 Unstart Modes in High-Speed Inlets (Tang et al., 2023)

Recent high-fidelity experiments involving compression ramp geometries at Mach numbers ranging from 6.5 to 8.3 have provided improved datasets (Lara et al., 2023), while

advances in numerical validation techniques (Park et al., 2023) have enhanced the modeling of SWBLI, enabling more accurate and physics-based predictive tools. Nevertheless, fully capturing the complex unsteady behaviors of SWBLI, particularly in realistic operational environments, remains an open and active area of research.

2.3 Controlling the Inevitable

Recent research efforts have increasingly focused on controlling SWBLI-induced separation and preventing unstart phenomena in hypersonic inlets. Flow control strategies developed for this purpose are broadly classified into two categories: passive and active control methods. Each approach offers distinct advantages and limitations depending on the specific flow environment and mission requirements.

Passive flow control techniques involve modifications to surface properties or the addition of geometric elements without the introduction of external energy into the system. Among the most widely studied passive methods are micro-vortex generators (MVGs) and micro-ramps, which introduce streamwise vortices into the boundary layer (Saad et al., 2012; Wang et al., 2022). These vortices transfer high-momentum fluid from outside the boundary layer toward the near-wall region, energizing the flow, preventing separation. Recent numerical investigations have indicated that mixed-orientation vortex generator arrays can outperform traditional single-orientation configurations, leading to improved uniformity in isolator flow fields and more effective suppression of flow separation (Khan et al., 2024).

In addition to vortex-based methods, riblet structures have also been explored. For instance, herringbone riblets, inspired by surface patterns found on sharks and birds, have demonstrated small but notable reductions in separation in SWBLI environments (Wen et al., 2024). Furthermore, surface condition studies reveal that smoother surfaces weaken SWBLI, leading to thinner boundary layers and reducing the likelihood of shock-induced separation (Garcia et al., 2022).

One of the most researched techniques in high-speed inlets is the boundary-layer bleed method, which actively removes low-momentum fluid through bleed slots or porous surfaces. This removal reduces the adverse pressure gradient imposed by the shock, stabilizes the boundary layer, minimizes thermal loads, and enhances inlet performance (Delery, 1985; Reinartz et al., 2003). Although bleed systems are widely adopted, their optimization remains an ongoing challenge due to the trade-offs between bleed mass flow rates and aerodynamic efficiency.

In contrast, active flow control techniques directly inject energy into the flow field to modify separation and shock behavior dynamically. Among the leading active methods are air-jet vortex generators (AJVGs) and microjet arrays, which introduce high-momentum jets into the boundary layer to generate counter-rotating vortex pairs (CVPs) (Ramaswamy & Schreyer, 2021; Sebastian & Schreyer, 2023; Wang et al., 2022). These CVPs increase the near-wall momentum, thus suppressing separation and delaying flow breakdown. Experimental and numerical studies have shown that AJVGs become particularly effective at Mach numbers above 2.7 (Ramaswamy & Schreyer, 2021; Wang et al., 2022), where flow conditions demand more energetic control measures. Additionally, spanwise-inclined AJVG

configurations have proven highly flexible, adapting well to both supersonic and hypersonic environments (Ramaswamy & Schreyer, 2021; Sebastian & Schreyer, 2023). Optimal jet spacing further enhances their effectiveness, balancing momentum addition with minimal flow disturbance (Wang et al., 2022).

2.4 Closure

In summary, the existing body of research highlights that while passive flow control methods offer the advantages of simplicity, robustness, and minimal energy consumption, they are generally limited in their ability to adapt to varying flight conditions. In contrast, active flow control techniques provide active adaptability and enhanced control authority but introduce additional system complexity, higher energy demands, and integration challenges (Gaitonde, 2015). Consequently, the selection of an appropriate flow control strategy must carefully balance these trade-offs, considering mission-specific requirements for aerodynamic performance, operational reliability, and overall system flexibility. This understanding forms the foundation for the present investigation, which seeks to further explore and optimize flow control approaches for effective management of shock wave–boundary layer interactions in high-speed applications.

Chapter 3

Computational Methodology

Computational methodology is the systematic approach used to simulate and analyze physical phenomena through mathematical modeling, discretization techniques, and various solvers. In fluid dynamics, it enables the prediction of complex flow behaviors, such as SWBLI, by solving governing equations under defined boundary and initial conditions. This methodology is necessary for flows that are difficult, expensive, or impractical to duplicate experimentally. It offers a controlled environment to study flow physics, design concepts, and evaluate performance parameters with high resolution and repeatability.

3.1 Geometry

The geometric configuration employed in this study is based on the inlet design proposed by (Fischer & Olivier, 2009). This configuration was selected due to its hypersonic flow capacity and operating freestream conditions of Mach 7.7. Using ANSYS DesignModeler, a two-dimensional model of the inlet and isolator was rendered. The major geometric elements, including the compression ramps, inlet duct, isolator section, and cowl structure, are detailed below.

3.1.1 Baseline Geometry

The inlet configuration employed in this study features a dual-ramp intake design. The first compression ramp is inclined at an angle of 9° relative to the horizontal axis and has a ramp run of 267.7 mm . Following the first ramp, the second compression ramp is inclined at a steeper angle of 20.5° , with a corresponding ramp length of 119.5 mm . These ramps are the primary compression mechanism of hypersonic inlets.

Extending from the end of the second ramp, a horizontal inlet section is introduced, spanning a length of 58.8 mm and maintaining alignment parallel to the freestream direction. This section serves to transition the compressed flow into the isolator, which follows immediately downstream. The isolator section, essential for stabilizing shock structures and maintaining inlet mass flow, is inclined slightly downward at an angle of -1° relative to the horizontal and extends over a length of 141.8 mm .

At the end of the isolator, the cowl structure is positioned vertically, beginning at a height of 17.9751 mm above the isolator surface. The cowl then extends horizontally toward the inlet direction, spanning a length of 206.8 mm while being parallel to the freestream. The complete two-dimensional base geometry, including all major features and sections, is illustrated in Figure 4.

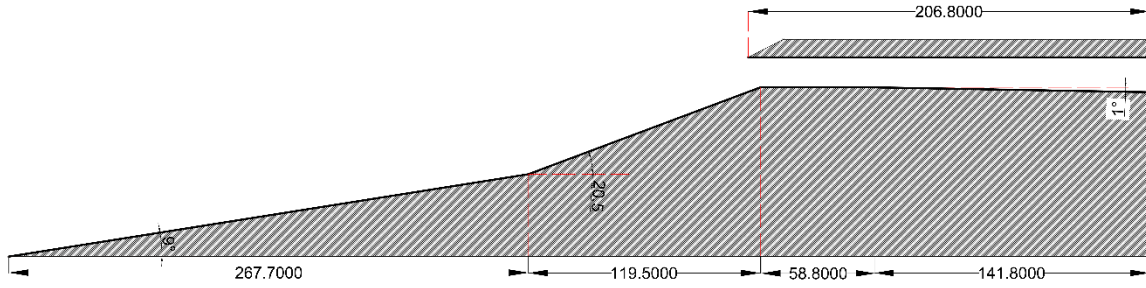


Figure 4 Baseline Geometry recreated from (Fischer & Olivier, 2009)

3.1.2 Bleed Slot Geometry

Following the validation of the base inlet, modifications were introduced to implement the boundary-layer bleed method. The overall geometry remained unchanged except within the inlet section of the hypersonic intake, where the bleed slot was integrated. This region was selected for modification because it hosts the strongest SWBLI, making it the critical location for separation control through boundary-layer bleed.

To optimize the bleed slot performance, three primary parameters were systematically studied: the slot location, slot inclination angle, and slot diameter. Previous literature provided baseline values for these parameters (G. J. Harloff & Smith, 1996; Schulte et al., 1998, 2001). Specifically, an inclination angle of 45° relative to the surface was identified for optimal performance (Schulte et al., 2001), and a slot diameter of 4.3275 mm was recommended (Schulte et al., 1998). However, for slot location, existing studies suggested positioning the bleed slot near the shock impingement point, but did not specify an exact distance (Schulte et al., 2001). Therefore, a more detailed parametric study was conducted in this work to close this knowledge gap.

For the bleed slot location optimization, the slot's distance was varied starting slightly upstream of the inlet's beginning (10.59 mm from the leading edge) and extending up to the end of the separation bubble observed in the base case (approximately 38.59 mm downstream). Throughout this location optimization phase, the slot angle and diameter were maintained at 45° and 4.3275 mm , respectively.

Once the optimal location was determined, the inclination angle of the bleed slot was further varied across a wide range, from 30° to 120° to evaluate the sensitivity of separation control to slot orientation. These simulations were conducted while maintaining the optimized location and the previously selected slot diameter.

Finally, after fixing the optimized location and inclination angle, the slot diameter was systematically varied to determine its influence on bleed effectiveness. This comprehensive multi-parameter investigation enabled the optimization of a bleed slot configuration that minimizes separation length and enhances overall inlet flow quality.

The final optimized two-dimensional geometry, incorporating the boundary-layer bleed slot and all major geometric features, is illustrated in Figure 5.

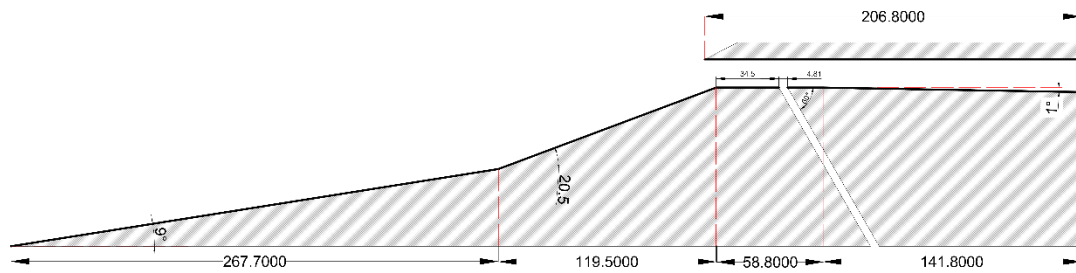


Figure 5 Baseline Geometry with Bleed Slot

3.2 Meshing

A structured grid topology was generated using ANSYS ICEM CFD to accurately capture boundary layer development, shock reflections, and separation behavior. Mesh generation efforts prioritized achieving high mesh quality and ensuring sufficient resolution in regions exhibiting strong gradients, particularly near walls and shock interaction zones.

Key mesh parameters were defined as follows:

- The non-dimensional wall distance (Y^+) was maintained within a range of 10 to 100 to ensure acceptable near-wall resolution without requiring full viscous sublayer resolution.
- The maximum aspect ratio of the mesh was targeted to be close to or below 1000, without exceeding practical computational resource limits.
- The orthogonal quality of the mesh was maintained above 0.3, while the overall mesh quality metric was kept higher than 0.97, ensuring minimal skewness and reducing numerical diffusion.

3.2.1 Baseline Meshing

To ensure the accuracy and reliability of the simulation results, a mesh independence study was conducted. Three different structured meshes, each with varying element densities, were generated to evaluate the influence of mesh refinement on the solution. This approach helps to confirm that the results are insensitive to further mesh refinement beyond a certain threshold, balancing accuracy with available computational resources while still satisfying the required meshing parameters.

The three mesh densities considered were as follows:

- **Coarse Mesh:** 299,482 nodes and 298,116 elements
- **Medium Mesh:** 360,297 nodes and 358,800 elements
- **Fine Mesh:** 402,270 nodes and 400,688 elements

Following simulations using these meshes allowed for the identification of an optimal mesh that achieves an acceptable trade-off between solution accuracy and computational cost.

3.2.2 Bleed Slot Meshing

To ensure consistency in mesh quality and maintain the validity of comparative results, both the baseline and bleed case simulations were constructed using meshes with approximately the same number of nodes and elements. This approach minimized grid-related discrepancies and ensured that any differences in flow behavior could be attributed to the physical effects of the bleed configuration rather than variations in numerical resolution.

3.3 Turbulence Models

In CFD, various turbulence models are utilized to simulate the complex behavior of turbulent flows efficiently and accurately. These models vary in quality, computational cost, and applicability depending on the flow characteristics and simulation objectives. The primary models considered in this study are described below.

3.3.1 Reynolds Averaged Navier Stokes (RANS) Model

RANS models are typically employed for steady-state simulations of turbulent flows. In this approach, the flow variables are decomposed into time-averaged and fluctuating components by applying time-averaging to the Navier–Stokes equations. This results in the appearance of a Reynolds stress term, which accounts for the effects of turbulence and requires closure using empirical turbulence models such as k- ϵ or k- ω .

RANS models are particularly effective for predicting mean flow characteristics, especially in wall-bounded flows, where they accurately capture the influence of turbulence without resolving individual eddies. They are computationally less expensive compared to higher-fidelity methods. However, RANS models may struggle in transient flows or highly complex geometries due to underlying assumptions that may not be valid under such conditions.

Equation 1 Reynolds Averaging

$$\rho = \bar{\rho} + \rho' \qquad U = \bar{U} + u' \qquad P = \bar{P} + p'$$

Equation 2 Continuity Equation

$$\frac{\partial \bar{\rho}}{\partial t} + \nabla \cdot (\bar{\rho} \bar{U}) = 0$$

Equation 3 Momentum Equation

$$\frac{\partial(\bar{\rho}\bar{U}_i)}{\partial t} + \nabla \cdot (\bar{\rho}\bar{U}_i\bar{U}) = -\frac{\partial\bar{P}}{\partial x_i} + \frac{\partial}{\partial x_j} \left[\mu \left(\frac{\partial\bar{U}_i}{\partial x_j} + \frac{\partial\bar{U}_j}{\partial x_i} \right) - \overline{\rho u'_i u'_j} \right]$$

Equation 4 Energy Equation

$$\frac{\partial(\rho e_t)}{\partial t} + \nabla \cdot [\vec{V}(\rho e_t + p)] = \nabla \cdot [k \nabla T + (\bar{\tau} \cdot \vec{V})] + \dot{S}_g$$

Equation 5 Boussinesq Hypothesis

$$-\overline{\rho u'_i u'_j} = \mu_t \left(\frac{\partial V_i}{\partial x_j} + \frac{\partial V_j}{\partial x_i} - \frac{1}{3} \frac{\partial V_k}{\partial x_k} \delta_{ij} \right) - \frac{2}{3} \rho k \delta_{ij}$$

Equation 6 Turbulent Viscosity relation to k and ω

$$\mu_t = \rho \frac{k}{\omega}$$

3.3.2 $k - \varepsilon$ Model

The $k-\varepsilon$ model utilizes two transport equations: one for turbulent kinetic energy (k) and another for the rate of dissipation (ε).

1. **Turbulent Kinetic Energy (k):** Quantifies the energy contained within turbulent eddies, serving as a measure of turbulence intensity in the flow.
2. **Dissipation Rate (ε):** Represents the rate at which turbulent kinetic energy is converted into thermal energy due to viscous effects, indicating the decay of turbulence.

The $k-\varepsilon$ model performs well in flows with strong streamline curvature and vortices; however, it tends to underperform near solid boundaries, where accurate near-wall modeling is critical.

3.3.3 $k - \omega$ Model

Similarly, the $k-\omega$ model employs two transport equations, solving for turbulent kinetic energy (k) and the specific dissipation rate (ω).

1. **Turbulent Kinetic Energy (k):** Quantifies the energy contained within turbulent eddies, serving as a measure of turbulence intensity in the flow.

$$\rho \frac{\partial k}{\partial t} + \rho U_i \frac{\partial k}{\partial x_i} = \frac{\partial}{\partial x_i} \left(\mu + \frac{\mu_t}{\sigma_k} \frac{\partial k}{\partial x_i} \right) + \mu_t \left(\frac{\partial U_i}{\partial x_j} + \frac{\partial U_j}{\partial x_i} \right) \frac{\partial U_i}{\partial x_j} - \rho k \omega \beta^*$$

2. **Specific Dissipation Rate (ω):** Defines the rate at which turbulent kinetic energy dissipates relative to the energy itself, making it particularly effective for modeling near-wall turbulence where sharp gradients exist.

$$\rho \frac{\partial \omega}{\partial t} + \rho U_i \frac{\partial \omega}{\partial x_i} = \frac{\partial}{\partial x_i} \left(\mu + \frac{\mu_t}{\sigma_\omega} \frac{\partial \omega}{\partial x_i} \right) + \alpha \mu_t \left(\frac{\partial U_i}{\partial x_j} + \frac{\partial U_j}{\partial x_i} \right) \frac{\partial U_i}{\partial x_j} - \beta \rho \omega^2$$

The k - ω model offers superior resolution of the near-wall region and is well-suited for applications involving adverse pressure gradients and boundary layer separation. However, it can exhibit sensitivity issues in the free-stream region, which may affect prediction accuracy in some cases.

3.3.4 Shear Stress Transport (SST) $k - \omega$ Model

The SST k - ω model is a hybrid model that combines the advantages of both the k - ω and k - ϵ models. It employs the k - ω model near walls to accurately resolve boundary layer effects and blends into the k - ϵ formulation in the free-stream region to reduce sensitivity issues. This approach enhances the model's robustness and accuracy in simulating flows involving separation, reattachment, and complex aerodynamic phenomena.

3.3.5 Large Eddy Simulation (LES)

LES focuses on resolving the larger eddies in turbulent flows, while modeling the smaller-scale motions using a subgrid-scale (SGS) model. This approach recognizes that large eddies carry the majority of turbulent kinetic energy and directly affect momentum and heat transfer, thus warranting explicit resolution.

The primary advantage of LES is its ability to produce high-fidelity representations of unsteady, complex turbulent flows. However, it demands significant computational power due to the fine spatial resolution needed to capture large eddies and their interactions across smaller scales. Thus, while LES provides deep insights into turbulence dynamics, its high computational cost often limits its use to fundamental research and high-priority engineering applications.

3.3.6 Detached Eddy Simulation (DES)

DES represents a hybrid modeling strategy that integrates RANS and LES methodologies. It applies RANS modeling in near-wall regions where turbulence is relatively stable and switches to LES in separated flow regions characterized by chaotic turbulence.

It successfully balances computational efficiency and flow detail resolution, capturing both steady and unsteady flow features. Nevertheless, the transition between RANS and LES zones can introduce challenges, particularly the so-called "grey area" problem, where neither model accurately captures the flow dynamics, potentially leading to local inaccuracies.

3.4 Flow Solver

In the present investigation, the RANS equations were solved using a density-based solver framework. ANSYS Fluent was utilized to perform the simulations, applying the higher-accuracy implicit solution method. Spatial discretization was achieved using a second-order accurate Advection Upstream Splitting Method (AUSM) scheme for robust shock capturing and improved resolution of high-gradient regions.

The fluid properties were defined based on standard models appropriate for high-speed aerodynamics. The density of air was described as an ideal gas, while the specific heat capacity at constant pressure (C_p) was specified using a piecewise-polynomial function. The dynamic viscosity was modeled using Sutherland's law to incorporate temperature dependence. Thermal conductivity and Molecular Weight were assumed to be constant.

Convergence criteria were carefully maintained to ensure residual reduction and solution stability across all mesh levels.

3.5 Boundary Conditions

The inlet and outlet boundaries were specified as a pressure far-field at the inlet and a pressure outlet at the exit. The flow was initialized with a Mach number of 7.7 at the inlet, with a gauge pressure of 750 Pa applied at both the inlet and outlet, and an operating pressure set to 0 Pa. The static temperature at both boundaries was maintained at 125 K. The turbulence properties at both the inlet and outlet were defined using a turbulent intensity of 0.08% and a hydraulic diameter of 0.0155 m (Fischer & Olivier, 2009).

The wall boundaries were modeled using the standard no-slip, adiabatic wall condition settings available in ANSYS Fluent.

For simulations involving bleed cases, the inlet and outlet boundary conditions remained unchanged. The bleed outlet was specified with the same pressure outlet conditions described previously (Schulte et al., 1998).

3.6 Validation of Numerical Model

The simulation model was validated by comparing the pressure coefficient (C_p) distribution along the bottom wall of the inlet with available experimental data. As illustrated in Figure 6, the computational results closely follow the overall trend of the experimental curve, demonstrating good agreement in the location of key flow features such as shock impingement and separation regions.

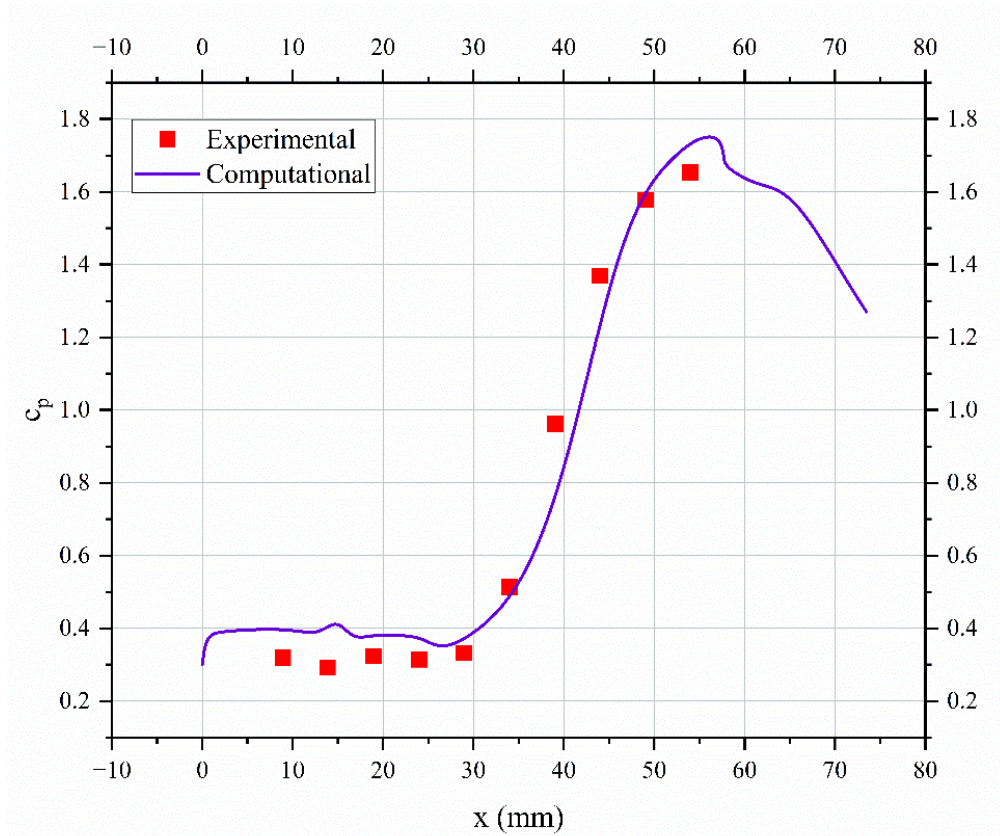


Figure 6 Validation of Numerical Model against Experimental Data from (Fischer & Olivier, 2009)

While minor deviations are observed between the numerical and experimental values, particularly in regions of steep pressure gradients, these differences are attributed to numerical modeling limitations, including discretization errors, turbulence model assumptions, and mesh resolution. Nonetheless, the validation confirms that the simulation framework is sufficiently accurate for analyzing shock-induced separation and evaluating flow control strategies.

3.6.1 Sensitivity Study

A turbulence model sensitivity study was performed to determine the most suitable modeling approach for capturing SWBLI effects, as illustrated in Figure 7. The models evaluated included the Standard $k-\epsilon$ model, the Realizable $k-\epsilon$ model, the RNG $k-\epsilon$ model, the Standard $k-\omega$ model, and the SST $k-\omega$ model. Among these, the Standard $k-\omega$ model provided the closest agreement with available experimental data, particularly in accurately

predicting boundary layer separation and reattachment behavior. Therefore, the Standard $k-\omega$ model was selected for all final simulation cases.

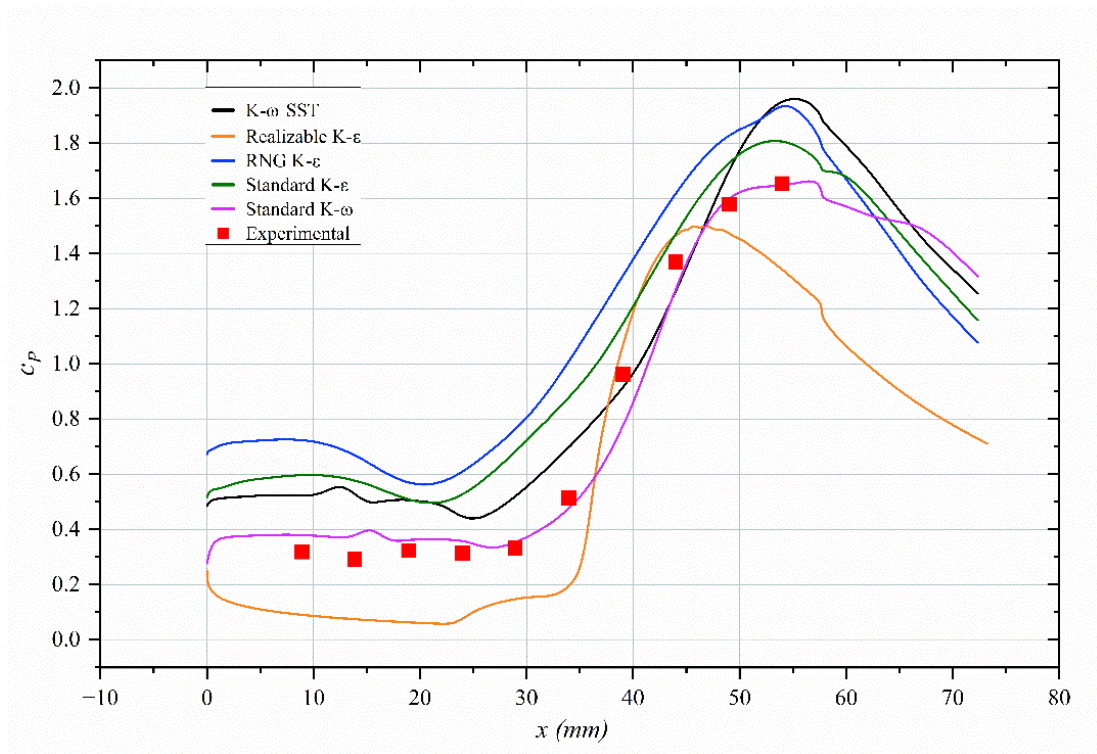


Figure 7 Sensitivity Analysis of Numerical Model

3.6.2 Grid Independent Study

To ensure numerical accuracy, a grid independence study was conducted using three meshes with increasing elements, illustrated in Figure 8. As defined in section 3.2.1. Each mesh was evaluated based on critical flow characteristics, including the separation bubble's size, the shock structures' position, and the distribution of wall pressure. Comparisons among these meshes confirmed mesh convergence, thereby validating the sufficiency of the selected grid resolution for accurate flow field prediction.

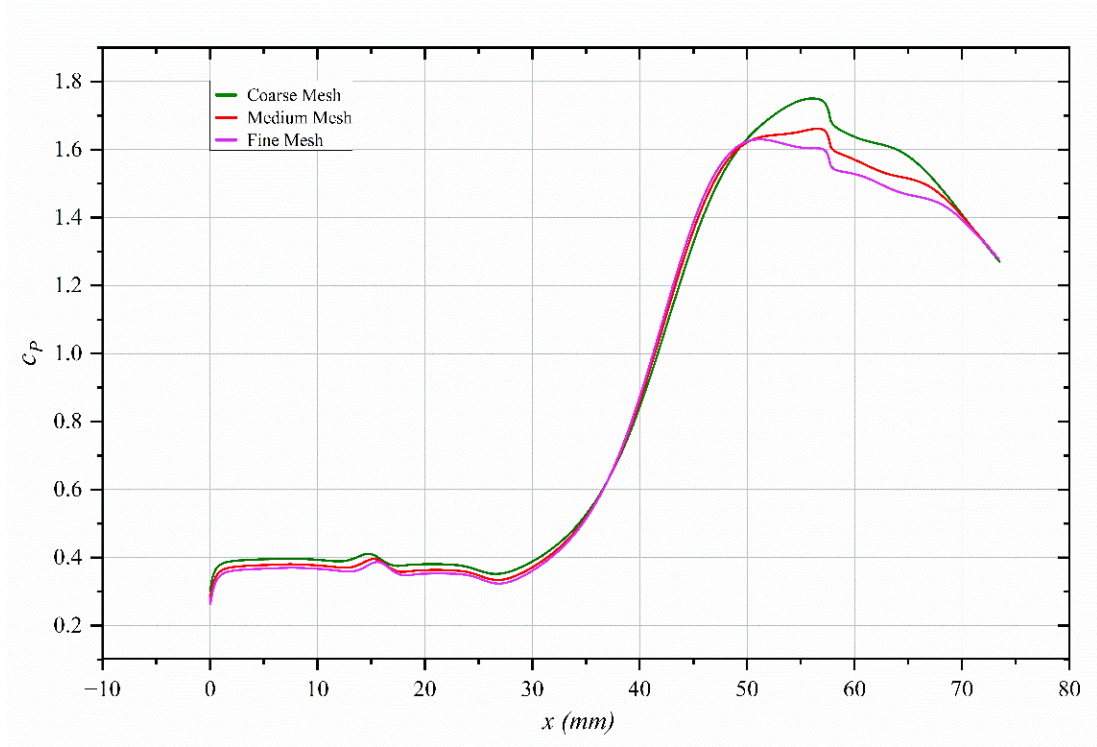


Figure 8 Grid Independent Study of Numerical Models

Chapter 4

Results and Discussion

4.1 Baseline Flow Analysis

Analysis of the schlieren image and Mach contour reveals the formation of a prominent separation bubble at the inlet, occupying approximately 70% of the inlet height, as illustrated in Figure 9. This region of flow separation significantly alters the internal aerodynamics and is a hallmark of strong SWBLI. The height of the separation bubble was quantified by isolating the corresponding temperature range, based on the thermal signature of the flow. Due to the intense thermal energy generated by the SWBLI, the temperature within the separation bubble was found to be approximately 860% higher than the freestream temperature, resulting in localized peaks between 1100K and 2100K. These high temperatures impose severe thermal stresses on the inlet surfaces, which, when coupled with the inherently unsteady nature of SWBLI, can severely degrade inlet performance and pose risks to structural integrity.

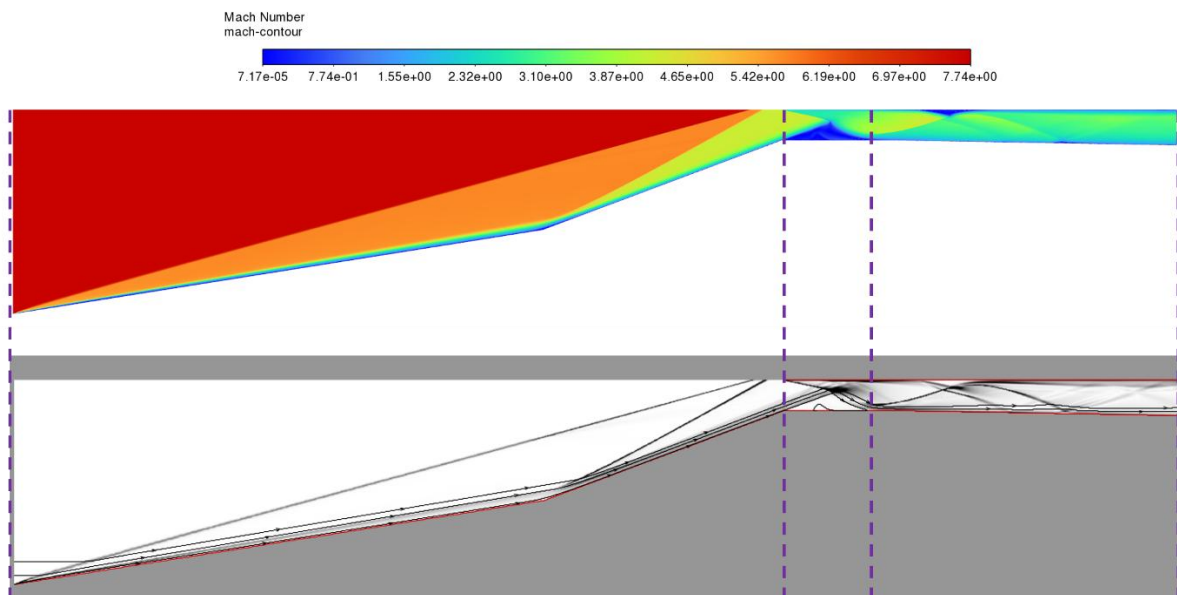


Figure 9 Top Image: Mach Contour; Bottom Image: Schlieren Image

This specific temperature range was therefore used in this study to accurately capture and visualize the height and extent of the separation bubble, as illustrated in Figure 10, both in the baseline case and in subsequent bleed optimization scenarios. The presence of the separation bubble leads to a reduction in effective flow area, commonly referred to as area contraction, which causes a loss of kinetic energy and a corresponding drop in total pressure. These effects directly impact the combustion efficiency of scramjet engines, ultimately reducing thrust and operational stability.

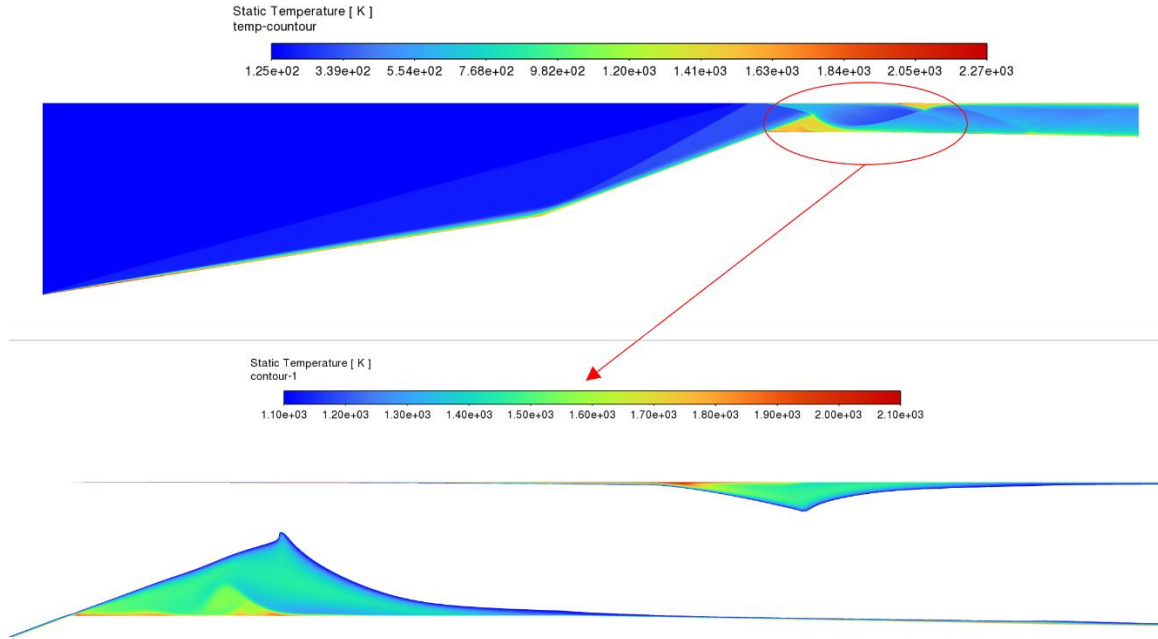


Figure 10 Top Image: Temperature Contour of Baseline Model; Bottom Image: Clipped Temperature Contour with Range (1100K to 1200K)

Additionally, reattachment shocks formed at the downstream edge of the separation bubble amplify the shock train system within the isolator, further intensifying pressure losses and velocity decay. Streamline plots from the baseline configuration highlight the formation of a primary vortex downstream of the shock impingement point. This vortex marks a critical turning region in the flow, often associated with the onset of expansion waves. This is corroborated by the velocity and density fields, as shown in Figure 11, which shows a localized drop in density as the flow accelerates.

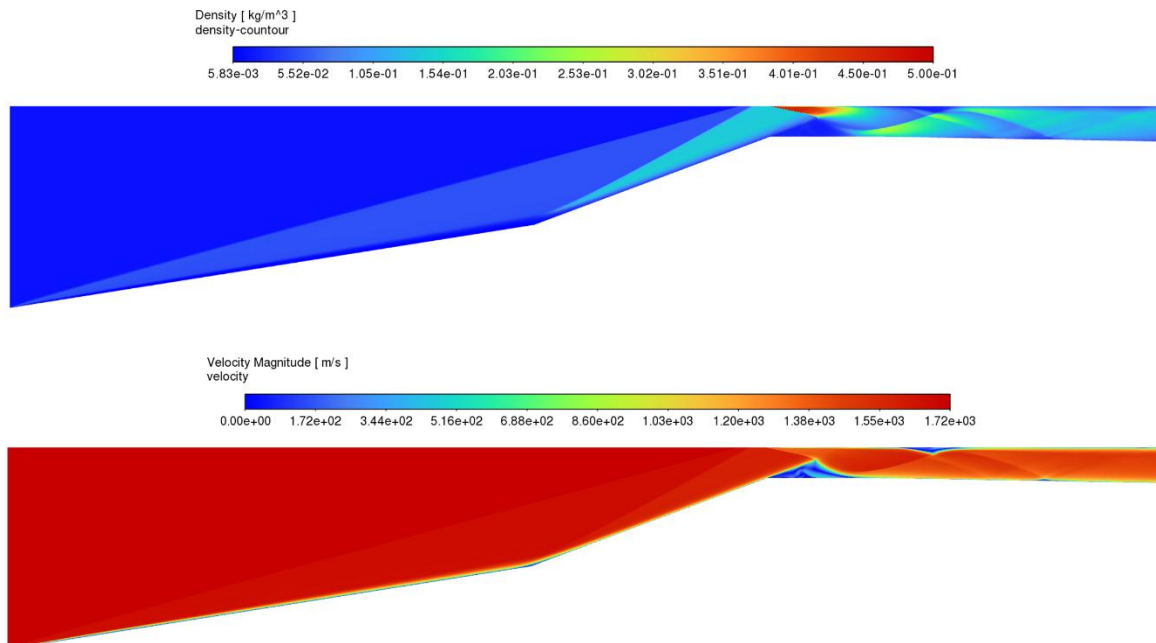


Figure 11 Top Image: Density Contour; Bottom Image: Velocity Contour

At the flow reattachment point, multiple weak compression waves are generated, curving the flow back toward the centerline. These waves gradually coalesce into a single, stronger compression structure, evident in the contours as a region of increasing density, ultimately forming the reattachment shock.

4.2 Bleed Slot Location Optimization

As detailed in section 3.1.2, the bleed slot location was systematically varied from 10.59 mm downstream of the inlet, starting from the estimated reattachment point at 38.59 mm. A total of twelve separate locations within this range were selected for analysis, with the in-between positions listed in Table 1.

Table 1 Bleed Slot Locations

Bleed Location from Ramp (mm)	Angle of Bleed Slot (°)	Width of the Bleed Slot (mm)
10.59	45	4.275
15.59	45	4.275
20.59	45	4.275
25.59	45	4.275
30.59	45	4.275
32.59	45	4.275
33.59	45	4.275
34.59	45	4.275
35.59	45	4.275
36.59	45	4.275
37.59	45	4.275
38.59	45	4.275

At each location, five key performance parameters were evaluated: total pressure recovery (π), mass flow rate ratio (Λ), and the separation bubble's height, length, and area. While all five metrics were computed, the primary focus of the optimization was placed on minimizing the geometric characteristics of the separation bubble, specifically its height, length, and area, due to their direct impact on inlet flow stability and performance. The variation of π and Λ are shown in Figure 12.

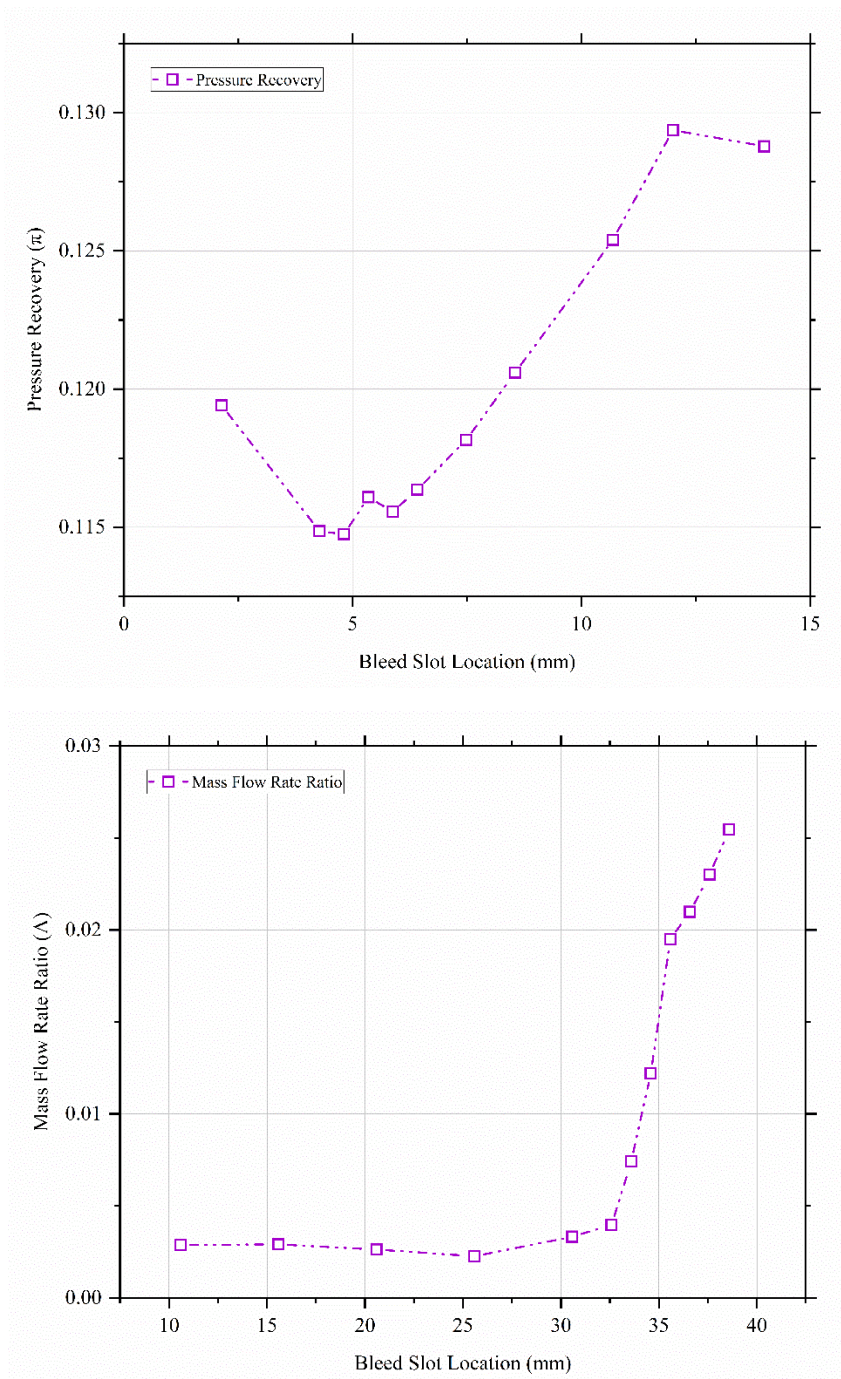


Figure 12 Top Graph: Bleed Slot Location vs π ; Bottom Image: Bleed Slot Location vs Λ

The results, illustrated in Figure 13, reveal a distinct low-value region where all three separation bubble parameters reach their minimum. This "bucket region" identifies the most effective bleed location range. Particularly, at 34.59 mm from the inlet start, the separation bubble height, length, and area were minimized to 3.32164 mm, 19.3087 mm, and 32.07 mm², respectively. The Mach contour overlaid with temperature contour in Figure 14 illustrates the reduction of the separation bubble size.

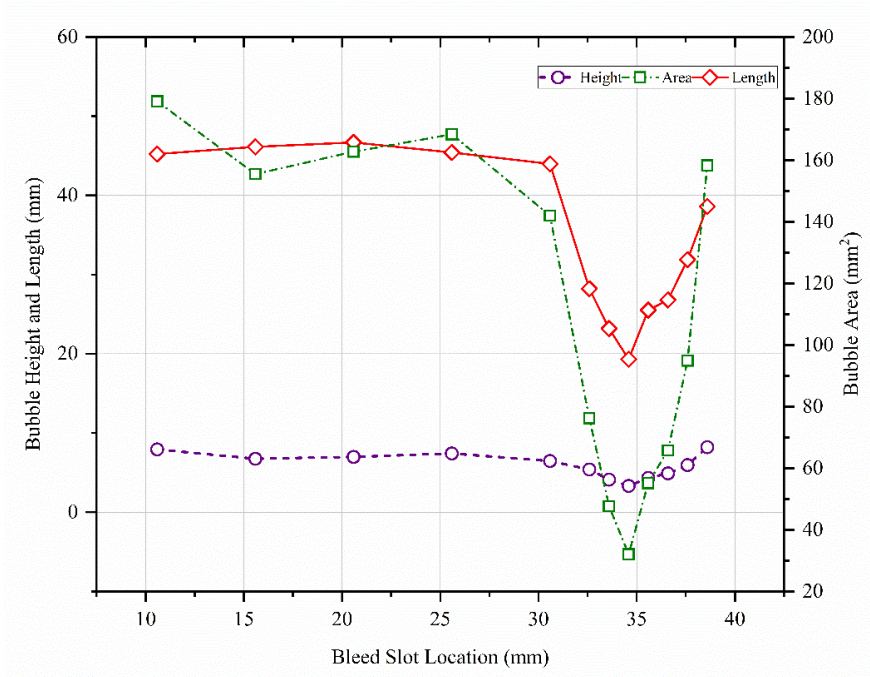


Figure 13 Bleed Location vs Bubble Height, Length, and Area

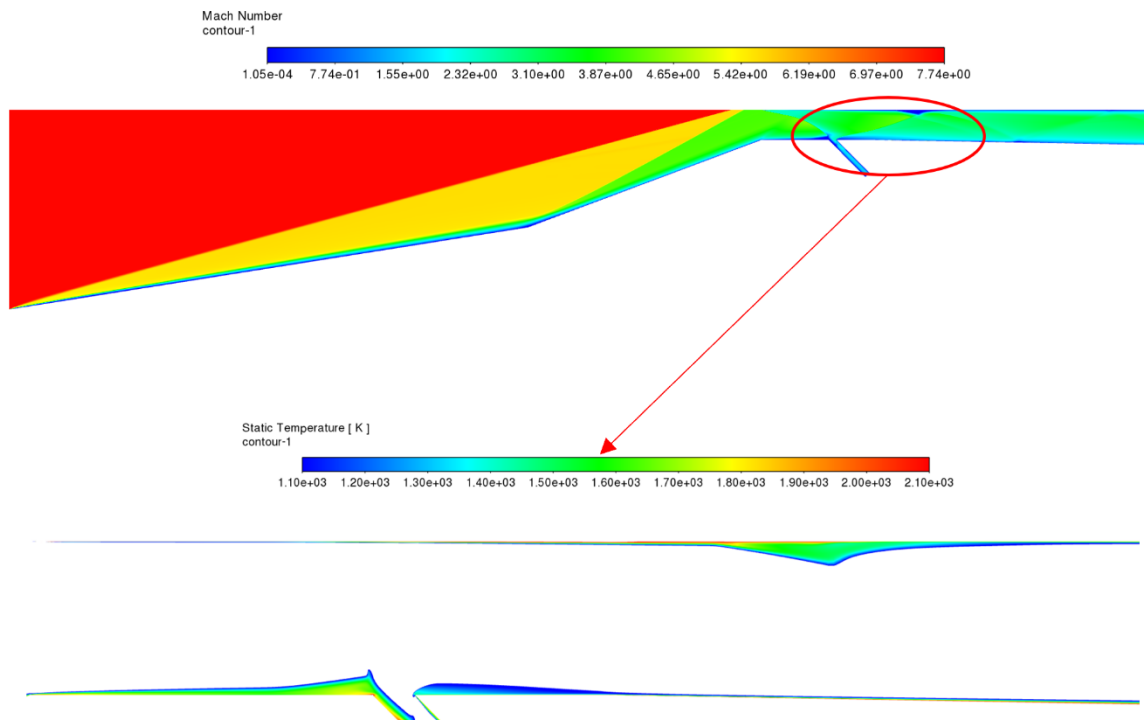


Figure 14 Top Image: Mach Contour; Bottom Image: Magnified Clipped Temperature Contour with Range (1100K to 2100K)

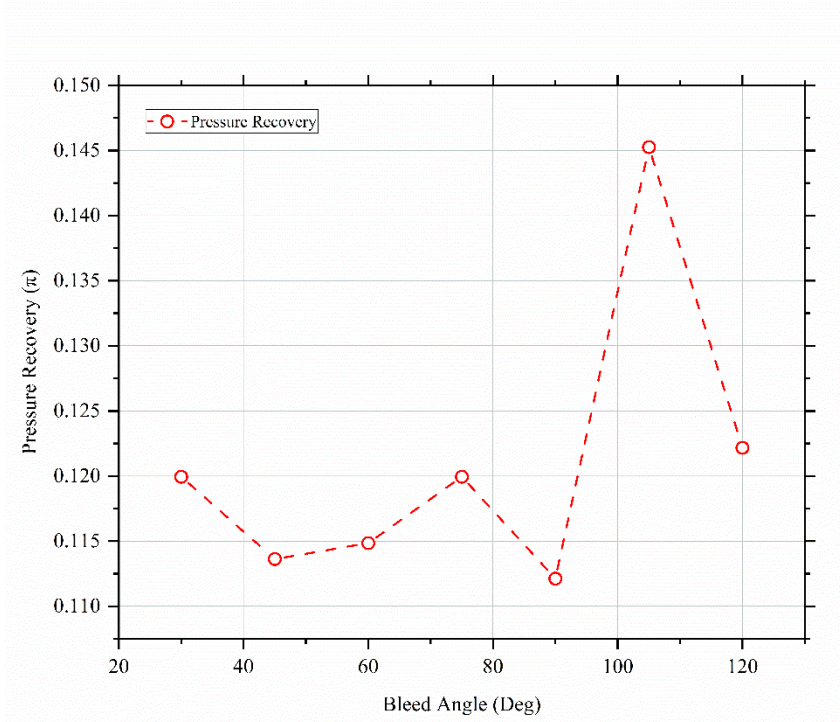
Following the identification of this optimal location, additional parametric studies were conducted to refine the bleed configuration. The bleed slot angle was first varied to assess its influence on bubble suppression, followed by a diameter-based study to determine the most effective geometric configuration for flow control.

4.3 Bleed Slot Angle Optimization

Following the bleed location study, the angle of the bleed slot was systematically varied to further refine the control configuration. Eight distinct bleed angles, ranging from 30° to 135°, were analyzed to evaluate their influence on shock-induced separation. The corresponding test cases and angle values are summarized in Table 2. The same five performance parameters: π , Λ , and the separation bubble's height, length, and area, were evaluated for each configuration, with primary emphasis on minimizing the bubble geometry. The variation of π and Λ are shown in Figure 15.

Table 2 Bleed Slot Angles

Bleed Location with Optimized Distance (mm)	Angle of Bleed Slot (°)	Width of the Bleed Slot (mm)
34.59	30	4.275
34.59	45	4.275
34.59	60	4.275
34.59	75	4.275
34.59	90	4.275
34.59	105	4.275
34.59	120	4.275
34.59	135	4.275



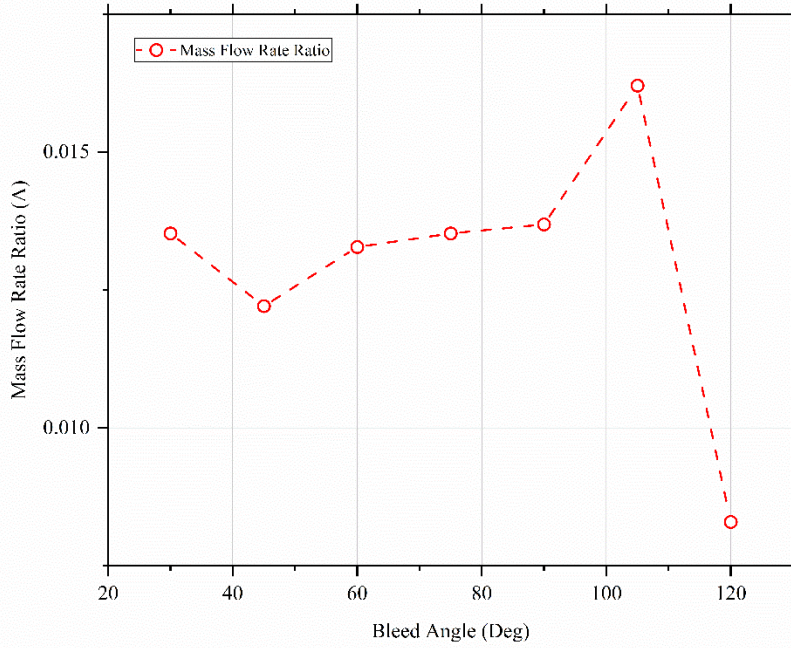


Figure 15 Top Graph: Bleed Slot Angle vs π ; Bottom Image: Bleed Slot Angle vs Λ

The results, illustrated in Figure 16, display a clear trend similar to the location optimization, with a defined drop or "bucket region" where all three separation bubble parameters reach their lowest values. The most effective bleed angle was identified as 60° , which yielded a separation bubble height of 3.03334 mm , a length of 17.3224 mm , and an area of 26.27 mm^2 . These results represent a deviation from previous findings reported in (Schulte et al., 2001), indicating that the optimal bleed angle may be highly geometry-specific. The Mach number contour overlaid with a clipped temperature field for this configuration is shown in Figure 17, clearly visualizing the improved flow uniformity and suppressed separation.

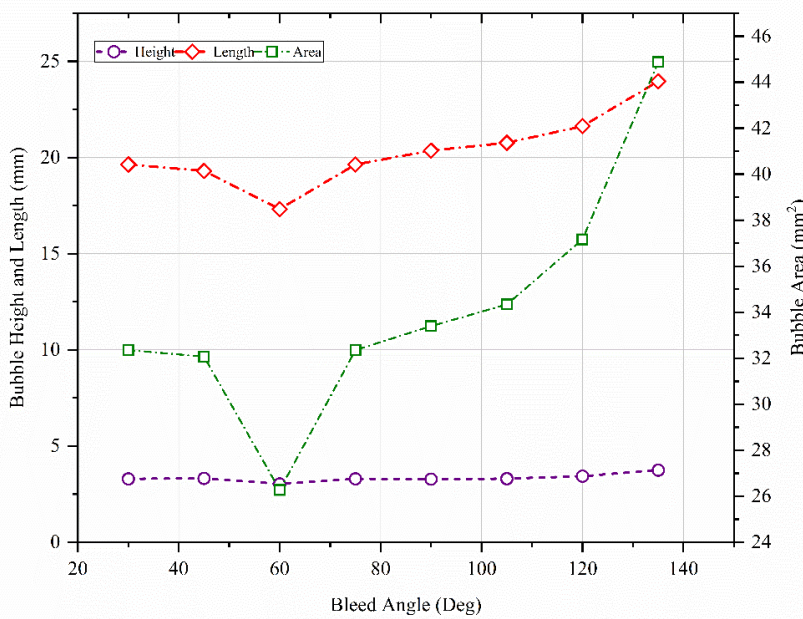


Figure 16 Bleed Angle vs Bubble Height, Length, and Area

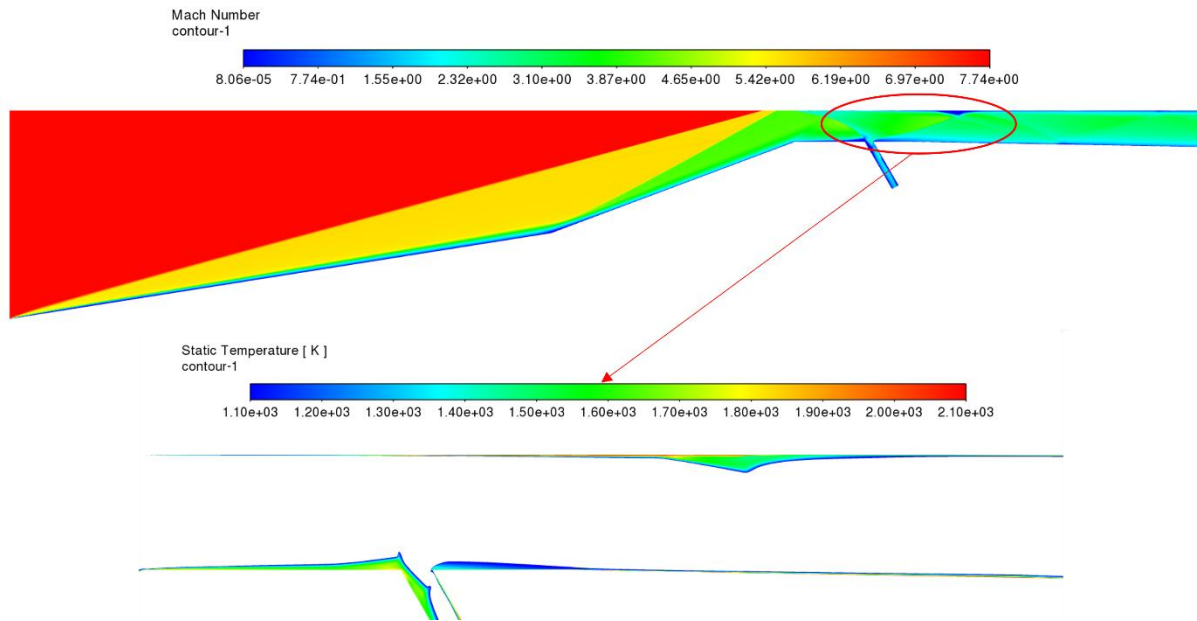


Figure 17 Top Image: Mach Contour; Bottom Image: Magnified Clipped Temperature Contour with Range (1100K to 2100K)

This optimized angle, in conjunction with the previously determined optimal location, was then used as the baseline for a subsequent study focusing on bleed slot diameter optimization.

4.4 Bleed Slot Diameter Optimization

Following the optimization of the bleed slot's location and angle, the final phase involved evaluating the effect of bleed slot diameter on flow separation control. In several prior studies (G. Harloff & Smith, 1995; Schulte et al., 2001, 2001), bleed diameter is typically defined as a fraction of the undisturbed boundary layer height. However, due to the numerical nature of this investigation, direct measurement of the undisturbed boundary layer height was not feasible. Therefore, the boundary layer height at the end of the second ramp was adopted as a practical reference for estimating the initial bleed diameter used in the earlier optimization steps.

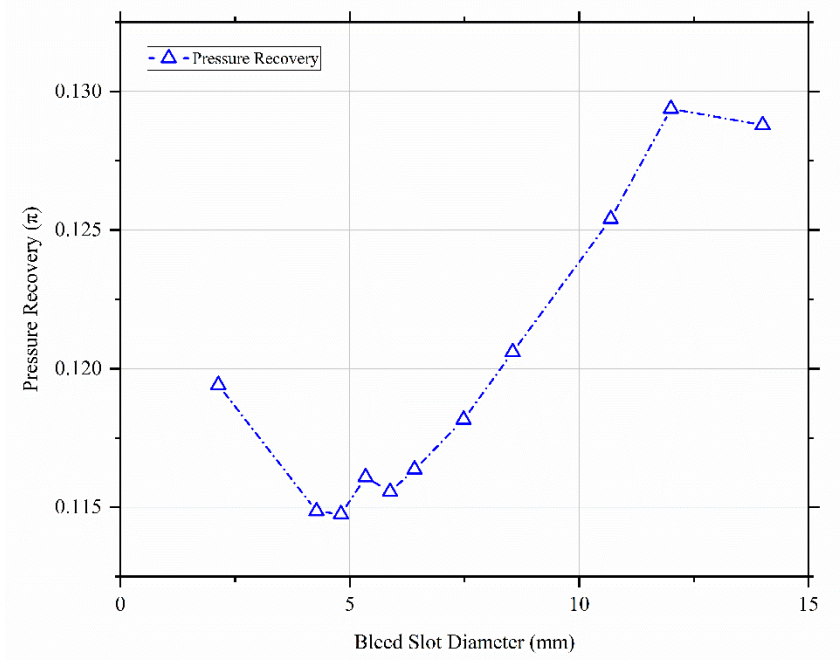
A total of eleven distinct bleed diameters, ranging from 2.1375 mm to 14 mm, were tested to assess their impact on shock-induced separation. These test configurations and corresponding diameter values are summarized in Table 3.

Table 3 Bleed Slot Diameter

Bleed Location with Optimized Distance (mm)	Angle of Bleed Slot (deg)	Width of the Bleed Slot (mm)
34.59	60	2.1375
34.59	60	4.275
34.59	60	4.809375
34.59	60	5.34375

34.59	60	5.878125
34.59	60	6.4125
34.59	60	7.48125
34.59	60	8.55
34.59	60	10.6875
34.59	60	12
34.59	60	14

As in the previous optimization stages, five performance metrics were evaluated for each case: π , Λ , and the separation bubble's height, length, and area. The primary focus remained on minimizing the geometric footprint of the separation bubble. The variations in π and Λ with respect to diameter, are shown in Figure 18.



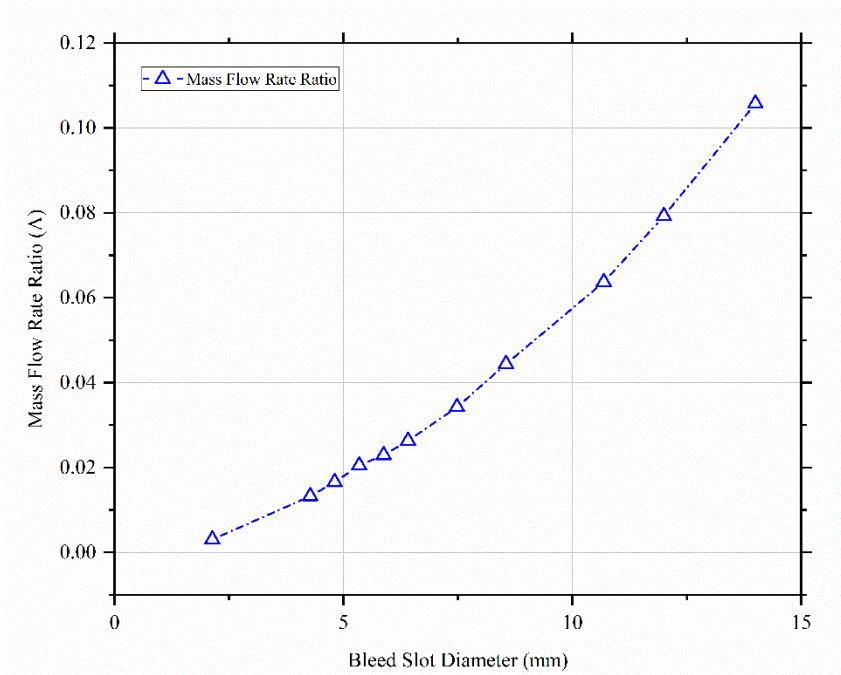


Figure 18 Top Graph: Bleed Slot Diameter vs λ ; Bottom Image: Bleed Slot Diameter vs π

Unlike the prior optimization cases, which exhibited a gradual "bucket" trend, this phase displayed a distinct behavior. The flow parameters experienced a sharp drop immediately after a diameter of approximately 4.2 mm, reaching a minimum before increasing linearly with further diameter enlargement, as illustrated in Figure 19.

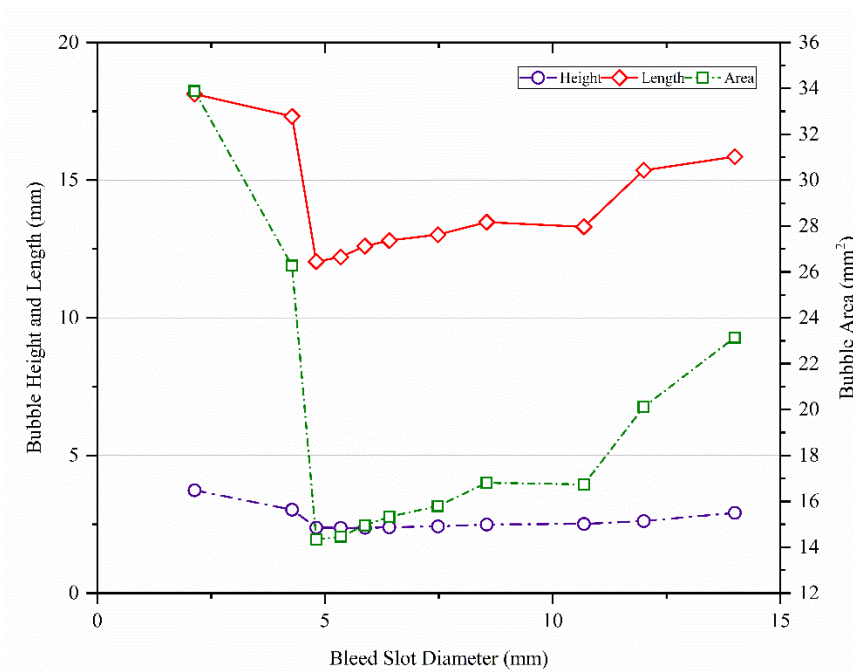


Figure 19 Bleed Diameter vs Bubble Height, Length, and Area

The most effective bleed diameter was found to be 4.809375 mm, corresponding to a separation bubble height of 2.3826 mm, a length of 12.0401 mm, and an area of 14.34 mm². This configuration achieved the greatest reduction in separation size while maintaining favorable pressure and mass flow characteristics. The Mach number contour

overlaid with a clipped temperature field for this configuration is shown in Figure 20, clearly visualizing the improved flow uniformity and suppressed separation.

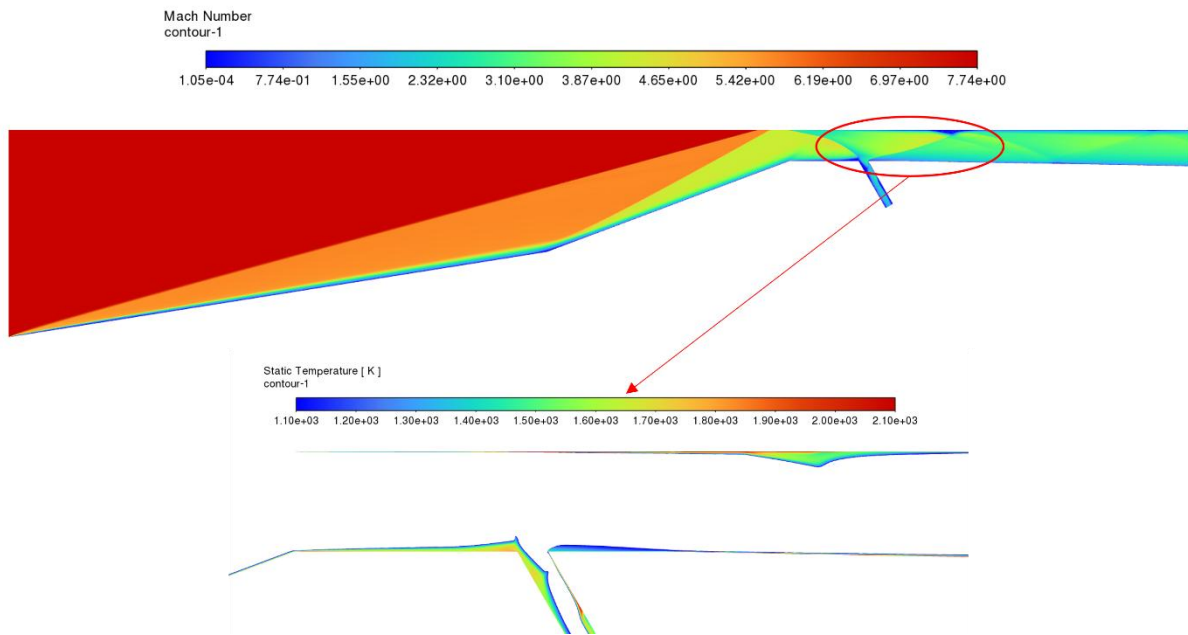


Figure 20 Top Image: Mach Contour; Bottom Image: Magnified Clipped Temperature Contour with Range (1100K to 2100K)

This study completes the optimization phase of the bleed slot configuration. The final optimized bleed geometry consists of a location 34.59 mm from the inlet start, an angle of 60° , and a diameter of 4.809375 mm .

Chapter 5

Conclusion

This study comprehensively investigated the dynamics of SWBLI in a hypersonic inlet using high-fidelity RANS simulations. The research was driven by the critical impact of SWBLI on the stability and performance of scramjet inlets, particularly within the isolator section, where confined interactions often lead to boundary layer separation, severe total pressure losses, and elevated thermal loads that can trigger inlet unstart.

Among the various flow control strategies, the boundary-layer bleed method was selected for its passive nature, robustness, and practical applicability in high-speed propulsion systems. A detailed parametric optimization was conducted to determine the most effective bleed slot configuration by varying three key geometric parameters: location, angle, and diameter. All simulations were performed under a freestream Mach number of 7.7, representative of realistic hypersonic flight conditions.

The baseline simulation revealed a substantial separation bubble forming near the inlet floor, reducing flow uniformity and increasing surface thermal stress. The introduction of a bleed slot significantly mitigated these effects. The optimized configuration, consisting of a bleed slot placed 34.59 mm downstream from the inlet start, angled at 60° , with a diameter of 4.809375 mm , achieved a reduction in the separation bubble height from 68% to 15% of the inlet height, along with a 94% decrease in total bubble area. This led to notable improvements in both total pressure recovery and flow uniformity across the inlet.

This work establishes a foundational understanding of bleed slot behavior and effectiveness in SWBLI control. It also highlights critical opportunities for future research. One potential direction includes reinjecting the bleed air upstream of the cowl shock to further energize the boundary layer, potentially reducing the strength of the shock train and improving overall pressure recovery. Additionally, extending the analysis to three-dimensional geometries could capture spanwise effects, further enhancing control fidelity. The integration of passive bleed with active flow control techniques, such as air-jet vortex generators, also presents a promising avenue for hybrid solutions, though such studies would require advanced three-dimensional experimental or computational capabilities.

In conclusion, this research contributes valuable insight into the control of hypersonic inlet SWBLI through bleed slot optimization and provides practical design recommendations for the development of more stable, efficient, and thermally resilient scramjet propulsion systems.

Chapter 6

References

- Babinsky, H., & Harvey, J. K. (2011). *Shock wave-boundary-layer interactions*. Cambridge university press.
- Babinsky, H., Li, Y., & Ford, C. W. P. (2009). Microramp Control of Supersonic Oblique Shock-Wave/Boundary-Layer Interactions. *AIAA Journal*, 47(3), 668–675.
<https://doi.org/10.2514/1.38022>
- Bogdonoff, S. M., Kepler, C. E., & Sanlorenzo, E. (1953). *A Study of Shock Wave Turbulent Boundary Layer Interaction at M=3* (No. 222; p. 77). Princeton University.
<https://apps.dtic.mil/sti/tr/pdf/AD0016740.pdf>
- Curran, E. T., & Murthy, S. N. B. (Eds.). (2000). *Scramjet propulsion*. American Institute of Aeronautics and Astronautics.
- Delery, J. M. (1985). Shock wave/turbulent boundary layer interaction and its control. *Progress in Aerospace Sciences*, 22(4), 209–280. [https://doi.org/10.1016/0376-0421\(85\)90001-6](https://doi.org/10.1016/0376-0421(85)90001-6)
- Dolling, D. S. (2001). Fifty Years of Shock-Wave/Boundary-Layer Interaction Research: What Next? *AIAA Journal*, 39(8), 1517–1531. <https://doi.org/10.2514/2.1476>
- Fischer, C., & Olivier, H. (2009, October 19). Experimental Investigation of the Internal Flow Field of a Scramjet Engine. *16th AIAA/DLR/DGLR International Space Planes and Hypersonic Systems and Technologies Conference*. 16th AIAA/DLR/DGLR International Space Planes and Hypersonic Systems and Technologies Conference, Bremen, Germany. <https://doi.org/10.2514/6.2009-7369>
- Gaitonde, D. V. (2015). Progress in shock wave/boundary layer interactions. *Progress in Aerospace Sciences*, 72, 80–99. <https://doi.org/10.1016/j.paerosci.2014.09.002>

- Garcia, M., Hoffman, E. N. A., LaLonde, E. J., Combs, C. S., Pohlman, M., Smith, C., Gragston, M. T., & Schmisser, J. D. (2022). Effects of Surface Roughness on Shock-Wave/Turbulent Boundary-Layer Interaction at Mach 4 over a Hollow Cylinder Flare Model. *Fluids*, 7(9), 286. <https://doi.org/10.3390/fluids7090286>
- Green, J. E. (1970). Interactions between shock waves and turbulent boundary layers. *Progress in Aerospace Sciences*, 11, 235–340. [https://doi.org/10.1016/0376-0421\(70\)90018-7](https://doi.org/10.1016/0376-0421(70)90018-7)
- Harloff, G. J., & Smith, G. E. (1996). Supersonic-inlet boundary-layer bleed flow. *AIAA Journal*, 34(4), 778–785. <https://doi.org/10.2514/3.13140>
- Harloff, G., & Smith, G. (1995, July 10). Numerical simulation of supersonic flow using a new analytical bleed boundary condition. *31st Joint Propulsion Conference and Exhibit*. 31st Joint Propulsion Conference and Exhibit, San Diego, CA, U.S.A. <https://doi.org/10.2514/6.1995-2759>
- Khan, M. S. H., Madabushi, K., Ghosh, S., Edwards, J. R., & Narayanaswamy, V. (2024). Numerical investigations of shock/boundary-layer interaction and control for Mach 2.5 flow in an axisymmetric inlet. *Aerospace Science and Technology*, 154, 109468. <https://doi.org/10.1016/j.ast.2024.109468>
- Lara, A. M. P., Barreta, L. G., Matos, P. A. D. S., Santos, R. D. O., Vilela, R. G., Cardoso, R. D. L., Marcos, T. V. C., Galvão, V. A. B., & Rolim, T. C. (2023). Experimental investigation of the shock wave/boundary layer interaction at a compression corner and an incident shock wave generator. *Aerospace Science and Technology*, 142, 108692. <https://doi.org/10.1016/j.ast.2023.108692>
- Park, Y., Nam, J., Kim, Y., Jun, D., Lee, B. J., & Lee, Y. J. (2023). Validation of numerical simulations for investigating flow control in hypersonic inlets. *Aerospace Science and Technology*, 140, 108452. <https://doi.org/10.1016/j.ast.2023.108452>

- Ramaswamy, D. P., & Schreyer, A.-M. (2021). Control of Shock-Induced Separation of a Turbulent Boundary Layer Using Air-Jet Vortex Generators. *AIAA Journal*, *59*(3), 927–939. <https://doi.org/10.2514/1.J059674>
- Reinartz, B. U., Herrmann, C. D., Ballmann, J., & Koschel, W. W. (2003). Aerodynamic Performance Analysis of a Hypersonic Inlet Isolator Using Computation and Experiment. *Journal of Propulsion and Power*, *19*(5), 868–875. <https://doi.org/10.2514/2.6177>
- Saad, M. R., Zare-Behtash, H., Che-Idris, A., & Kontis, K. (2012). Micro-Ramps for Hypersonic Flow Control. *Micromachines*, *3*(2), 364–378. <https://doi.org/10.3390/mi3020364>
- Sabnis, K., & Babinsky, H. (2023). A review of three-dimensional shock wave–boundary-layer interactions. *Progress in Aerospace Sciences*, *143*, 100953. <https://doi.org/10.1016/j.paerosci.2023.100953>
- Schulte, D., Henckels, A., & Neubacher, R. (2001). Manipulation of Shock/Boundary-Layer Interactions in Hypersonic Inlets. *Journal of Propulsion and Power*, *17*(3), 585–590. <https://doi.org/10.2514/2.5781>
- Schulte, D., Henckels, A., & Wepler, U. (1998). Reduction of shock induced boundary layer separation in hypersonic inlets using bleed. *Aerospace Science and Technology*, *2*(4), 231–239. [https://doi.org/10.1016/S1270-9638\(98\)80001-1](https://doi.org/10.1016/S1270-9638(98)80001-1)
- Sebastian, R., & Schreyer, A.-M. (2023, January 23). Control of SWBLI in a 24deg Compression Ramp Flow with Air-jet Vortex-generator. *AIAA SCITECH 2023 Forum*. AIAA SCITECH 2023 Forum, National Harbor, MD & Online. <https://doi.org/10.2514/6.2023-2138>
- Sepahi-Younsi, J., Forouzi Feshalami, B., Maadi, S. R., & Soltani, M. R. (2019). Boundary layer suction for high-speed air intakes: A review. *Proceedings of the Institution of*

- Mechanical Engineers, Part G: Journal of Aerospace Engineering*, 233(9), 3459–3481. <https://doi.org/10.1177/0954410018793262>
- Souverein, L. J., Dupont, P., Debiève, J.-F., Dussauge, J.-P., Van Oudheusden, B. W., & Scarano, F. (2010). Effect of Interaction Strength on Unsteadiness in Shock-Wave-Induced Separations. *AIAA Journal*, 48(7), 1480–1493. <https://doi.org/10.2514/1.J050093>
- Tang, X., Fan, X., Xiong, B., Chen, L., & Chen, J. (2023). Study of multiple solution phenomenon for hypersonic air inlet. *Aerospace Science and Technology*, 136, 108236. <https://doi.org/10.1016/j.ast.2023.108236>
- Tang, X., Xiong, B., Fan, X., Liu, J., & Zhao, J. (2024). Experimental research on the flow mechanism of dual-separation unstart phenomenon in hypersonic inlet. *Aerospace Science and Technology*, 150, 109189. <https://doi.org/10.1016/j.ast.2024.109189>
- Wang, Z., Chang, J., Kong, C., Huang, R., & Xin, X. (2022). Experimental investigation of micro-ramp control for shock train under various incoming flow conditions. *Physical Review Fluids*, 7(10), 103401. <https://doi.org/10.1103/PhysRevFluids.7.103401>
- Wen, B., Zhong, S., Wang, G., & Li, L. (2024). Effects of herringbone riblets on shock-wave/turbulent boundary-layer interactions. *Aerospace Science and Technology*, 146, 108914. <https://doi.org/10.1016/j.ast.2024.108914>
- Xu, S., Wang, Y., Wang, Z., Fan, X., & Xiong, B. (2022). Experimental investigations of hypersonic inlet unstart/restart process and hysteresis phenomenon caused by angle of attack. *Aerospace Science and Technology*, 126, 107621. <https://doi.org/10.1016/j.ast.2022.107621>
- Zhang, Y., Chen, M., Wang, Z., Pang, M., Tan, H., Zhu, H., & Wang, M. (2025). Experimental investigation of the control of shock/boundary layer interaction based

on dynamic vortex generator. *Aerospace Science and Technology*, 162, 110175.

<https://doi.org/10.1016/j.ast.2025.110175>